


**Stable holey two-dimensional C<sub>2</sub>N structures with tunable electronic structure**

R. Longuinhos\* and J. Ribeiro-Soares

*Departamento de Física, Universidade Federal de Lavras, 37200-000 Lavras, Minas Gerais, Brazil* (Received 18 December 2017; revised manuscript received 19 April 2018; published 11 May 2018)

C<sub>2</sub>N holey two-dimensional crystals, or C<sub>2</sub>N-h2D, a recently synthesized carbon nitride layered material, show promising properties for electronic devices, highly selective molecular filters, and supercapacitors. Few studies have investigated the stacking order in C<sub>2</sub>N-h2D, which is fundamental to determine its optical activity and plays an important role in its band gap and in the diffusion barrier for ions and molecules through its structure. In this work, we investigate the phonon stability of several bulk C<sub>2</sub>N-h2D polytypes by using first-principles calculations. Among the polytypes addressed, only one does not display phonon instabilities and is expected to be observed in equilibrium. The electronic structure evolution of dynamically stable C<sub>2</sub>N-h2D from monolayer to bilayer and to bulk is unveiled. The direct band gap at  $\Gamma$  can be decreased by 34% from monolayer to bulk, offering opportunities for tuning it in optoelectronics. In addition, the effective masses of both carriers become smaller as the number of layers increases, and their anisotropy along in-plane directions displayed in the monolayer is reduced, which suggest that the carrier mobility may be tuned as well. These effects are then explained according to the interaction of the orbitals in neighboring layers. The results presented here shed light on the geometry and electronic structure of an emerging layered material due to its specific stacking and increasing number of layers and suggest new perspectives for applications in optoelectronics.

DOI: [10.1103/PhysRevB.97.195119](https://doi.org/10.1103/PhysRevB.97.195119)**I. INTRODUCTION**

The breakthrough of graphene [1–3] and the subsequent development of the field of two-dimensional materials [4–6] revealed the observation of a rich new chemistry and physics in the few-layer regime in comparison to the layered bulk counterpart. The new properties observed are promising for advances in the fields of electronics, optoelectronics [7–9], thermoelectrics [10,11], and clean-energy generation [12,13]. Graphene-based materials, such as graphene-oxide [14] and graphene-nitride composites [15], are under intense research. Besides their ease for use in large-scale production, they are easily incorporated into advanced functional materials, improving the physical properties of the resulting composite for applications such as energy storage and generation, sensor fabrication, and catalysis.

Layered carbon nitrides, or (graphitic) carbon IV nitrides, g-C<sub>3</sub>N<sub>4</sub>, can be viewed as *s*-triazine or tri-*s*-triazine (so-called melem) linked subunits, stacked in a specific order; first-principles calculations predict that stacked tri-*s*-triazine layers with space group *Cmc*2<sub>1</sub> are more stable than *s*-triazine-based g-C<sub>3</sub>N<sub>4</sub> [16–18]. A broad theoretical study predicted new semiconductor and metallic monolayer graphitic nitrides g-C<sub>x</sub>N<sub>y</sub> [19], with nitrogen atoms at the graphitic, pyridinic, or pyrrolic sites. Some of these materials were suggested as the geometries of synthesized graphitic nitrides: the tri-*s*-triazine-based g-C<sub>3</sub>N<sub>4</sub> [20] and the *s*-triazine-based g-CN (the experiments did not excluded the *s*-triazine-based g-C<sub>3</sub>N<sub>4</sub>) [21].

Recently, a new phase of layered carbon nitride was synthesized (at the time not yet predicted), whose empirical formula is

C<sub>2</sub>N. As the structure displays holes, the authors named it C<sub>2</sub>N holey two-dimensional crystal, or C<sub>2</sub>N-h2D [22]. Many-layer C<sub>2</sub>N-h2D is a semiconductor, with a band gap of 1.96 eV [22], and can be viewed as stacked atomic layers formed by pyrazine rings linked by C-C bonds to each other, as shown in Fig. 1.

C<sub>2</sub>N-h2D thin, flexible, many-layer films were solution processed for proof-of-concept field-effect transistor (FET) devices. The active channel composed of C<sub>2</sub>N-h2D crystal flakes, with an average thickness of  $8.0 \pm 3.5$  nm (many layers thick), transferred on top of a SiO<sub>2</sub>/Si wafer substrate, has a high on-off ratio ( $10^7$ ; Si-based FET devices have an on-off ratio of  $10^5$ ) but low mobilities ( $10^{-2}$  cm<sup>2</sup> V<sup>-1</sup> s<sup>-1</sup>) [22]. We note that early MoS<sub>2</sub>-based FET devices with bottom-gate geometries have poor mobilities ( $\approx 10^{-1}$  cm<sup>2</sup> V<sup>-1</sup> s<sup>-1</sup>) [23], while in the top-gate configuration mobilities were higher ( $\approx 10^2$  cm<sup>2</sup> V<sup>-1</sup> s<sup>-1</sup>) [24]. Furthermore, the nanoporous and layered structure of C<sub>2</sub>N-h2D is envisioned for supercapacitor [25] and molecular sieve [26–29] applications.

Most of the theoretical studies concerning C<sub>2</sub>N-h2D have focused on the monolayer physical properties, such as the mechanical [26,30] and thermal [30,31] properties, and tuning its electronic and optical properties by alloying [32] and strain engineering [30,33].

Few studies have investigated the bulk C<sub>2</sub>N-h2D geometries, a topic of paramount importance. To the best of our knowledge, there is no literature concerning the phonon stability of stacking geometries for bulk C<sub>2</sub>N-h2D, a very relevant topic, as only dynamically stable geometries are expected to be observed in equilibrium.

Here we study the phonon stability of several bulk C<sub>2</sub>N-h2D polytypes by using first-principles calculations. Among the polytypes addressed, only one, previously unknown and named AB'' here, does not display phonon instabilities and is expected

\*raphael.lobato@dfi.ufla.br

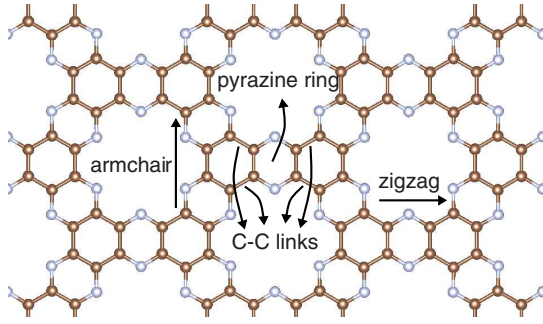


FIG. 1. Monolayer  $C_2N$ -h2D viewed as formed by pyrazine rings linked by C-C bonds to each other. Carbon and nitrogen atoms are represented as brown (dark gray) and light blue (light gray) balls, respectively.

to be observed in equilibrium under standard conditions. The electronic structures of the dynamically stable monolayer, bilayer, and bulk geometries of  $C_2N$ -h2D are investigated and found to be highly dependent on the number of layers. The direct band gap at  $\Gamma$  decreases from monolayer to bulk  $AB''$ , opening opportunities to explore the band gap engineering by controlling the number of layers in optoelectronic applications. Furthermore, the effective masses of both electrons and holes become smaller and more isotropic along in-plane directions as the number of layers increases. This suggests that the transport of the carriers may be tuned by controlling the number of layers and the direction in devices. Both band gap and effective-mass changes are explained in terms of the interaction of the orbitals in adjacent layers.

This paper is organized as follows: in Sec. II we describe the methods used. In Sec. III A we discuss the results for the structural parameters, the interlayer binding energies, and the lattice dynamics of the addressed geometries; in Sec. III B we discuss the evolution of the electronic structure from monolayer to bilayer and to bulk dynamically stable geometries. In Sec. IV we summarize the main conclusions on the electronic structure tunability for the dynamically stable polytype according to the number of layers and perspectives for use in optoelectronics.

## II. METHODS

First-principles calculations were performed using density-functional theory (DFT) [34,35] and density-functional perturbation theory (DFPT) [36] as implemented in the Plane-Wave Self-Consistent Field (PWSCF) and PHONON packages of the QUANTUM ESPRESSO distribution [37]. The Brillouin zone integrations on the electron wave vector were performed within the Monkhorst-Pack scheme [38] using  $\Gamma$ -centered grids of  $8 \times 8 \times 6$  for bulk and  $8 \times 8 \times 1$  for bilayer and monolayer systems. The two latter systems were treated within the slab model, with images separated by at least  $14 \text{ \AA}$  of vacuum space. For lattice and atomic position optimization, convergence was achieved for forces and stress lower than  $0.1 \text{ mRy/bohr}$  and  $50 \text{ MPa}$ , respectively.

Vibrational frequencies were computed using DFPT. In these calculations, the exchange-correlation energy is evaluated within the local-density approximation (LDA), with the Perdew-Zunger parametrization [39]. The valence electron-ion

interaction is described using the Troullier-Martins formulation for norm-conserving pseudopotentials [40]. The plane-wave kinetic-energy cutoff to describe the electronic wave functions (charge density) was set to  $64 \text{ Ry}$  ( $256 \text{ Ry}$ ). The phonon dispersions were calculated from the interatomic force-constant matrix, obtained from the dynamical matrices at the phonon wave vector in grids of  $2 \times 2 \times 2$  and  $4 \times 4 \times 1$  for bulk and bilayer, respectively. We note that LDA results for the lattice dynamics are in excellent agreement with the experimental values for the lattice vibration in crystals [41]. Even for interlayer rigid modes in layered materials, where the van der Waals (vdW) forces play an important role in the interlayer interactions, LDA provides an excellent description of the phonon frequencies in comparison to experiments, such as in h-BN, where the agreement is within 1% [42–44]. LDA predicts phonon energies in layered materials in better agreement with experiments than some functionals that better describe the correct physics of the dispersion interactions among the layers, such as the self-consistent nonlocal vdW-DF and vdW-DF2 functionals (as shown in the literature for  $MoS_2$ ,  $WSe_2$ , and graphite) [45,46]. A recent study of the lattice vibrational frequencies calculated by both the revised Vydrov and Van Voorhis nonlocal functional (rVV10) [47] and LDA for graphite showed that these functionals leads to comparable results for both intralayer and interlayer vibrations, where rVV10 is slightly closer to the experimental values for the intralayer vibrations, while LDA is slightly closer to the experimental values for the interlayer rigid modes [48]. This unexpected success of LDA may be due to the good description of the derivative of the forces with respect to atomic displacements [45] and to error cancellation [48].

For the study of the binding energies  $E_n$  in the different stacking phases in bulk and bilayer  $C_2N$ -h2D, we use the rVV10 functional, where the vdW interaction is described by a nonlocal and self-consistent term [49]. In these calculations, the valence electron-ion interaction is described by using the projector augmented-wave potentials [50,51]. The plane-wave kinetic-energy cutoff to describe the electronic wave functions (charge density) was set to  $38 \text{ Ry}$  ( $304 \text{ Ry}$ ). We express  $E_n$  values normalized by the number of van der Waals gaps in the unit cell  $n^{\text{vdW}}$  (for bilayer,  $n^{\text{vdW}} = 1$ , and in bulk  $n^{\text{vdW}} = 2$ ):

$$E_n = [E(\text{bulk/bilayer}) - 2E(\text{monolayer})]/n^{\text{vdW}}.$$

Throughout this work, the space-group number and its Schönflies notation are given according to the *International Tables for Crystallography* [52].

## III. RESULTS AND DISCUSSION

### A. Stability and structural information

The monolayer  $C_2N$ -h2D primitive unit cell has 12 carbon and 6 nitrogen atoms and has the symmetries of the hexagonal symmorphic space group  $P6/mmm$  (No. 191 or  $D_{6h}^1$ ). The experimental in-plane lattice parameter is  $8.24(96) \text{ \AA}$  [22]. In-plane lattice parameters in layered materials are systematically underestimated by LDA and overestimated by the generalized gradient approximation (GGA) and vdW functionals, and generally, LDA is in better agreement with experiments. Our results show that LDA underestimates the experimental value

TABLE I. Lattice parameters of monolayer (L1), AB'' bilayer (L2), and bulk C<sub>2</sub>N-h2D.

	LDA			rVV10			Expt. [22]	
	<i>a</i>	<i>b</i>	<i>c</i>	<i>a</i>	<i>b</i>	<i>c</i>	<i>a</i>	<i>c</i>
L1	8.202	<i>a</i>		8.316 <sup>a</sup>	<i>a</i>		8.24(96)	
L2	8.192	8.198		8.310	8.315			
Bulk	8.185	8.198	5.949	8.300	8.312	6.120	6.55(1) <sup>b</sup>	

<sup>a</sup>DFT-D2: 8.33 Å [29,53], 8.32 Å [27]; vdW-DF: 8.35 Å [28].

<sup>b</sup>Interlayer spacing  $d_{\text{Exp}}^{\text{vdW}} = 3.27\text{--}3.28$  Å (we assume  $c = 2d_{\text{Exp}}^{\text{vdW}}$ ) [22]; this work:  $d_{\text{LDA}}^{\text{vdW}} = 2.97$  Å,  $d_{\text{rVV10}}^{\text{vdW}} = 3.10$  Å.

by  $-0.4\%$  and rVV10 overestimates the experimental value by  $0.9\%$ . A comparison between the rVV10 results and other vdW functional results (DFT-D2 and vdW-DF) from the literature shows that rVV10 is in better agreement with experiments (L1 data in Table I).

To date, there are few data on the stacking geometry of the layers in bulk C<sub>2</sub>N-h2D and the phonon stability of possible polytypes. In order to shed light on the subject, we analyze the lattice vibrations for several stacking geometries of bulk C<sub>2</sub>N-h2D.

The vibrations of crystals can be described by phonon waves expressed as  $A \exp[i(\mathbf{k} \cdot \mathbf{r} - \omega t)]$ . A dynamically unstable stacking displays at least one phonon pattern associated with an imaginary eigenfrequency, and the atomic displacement is not a vibration; these are also called soft modes or phonon instabilities and are involved in phase transitions. For example, the AB orthorhombic graphite, which displays phonon instabilities [54,55], is predicted to occur in the phase-transition path from AB hexagonal graphite to diamond (under high pressure and temperature) [56]. A comparison of the interlayer binding energies among dynamically stable configurations provides an estimation of which one is more likely to occur. However, it does not provide any information regarding which one will display phonon instabilities. Indeed, dynamically stable and dynamically unstable geometries of ordered graphite display comparable values for interlayer binding energies [54,55].

We consider the stacking configurations AA [space group (SG)  $D_{6h}^1$ ], AB (SG  $D_{6h}^4$ ), and AB' (SG  $D_{2h}^{23}$ ) [53]. In the AA stacking the bottom and top layers of the unit cell are separated by a translation along the stacking direction. By translating one of the layers of the AA stacking along  $\hat{x} = (\hat{a} - \hat{b})/\sqrt{2}$  (zigzag) or  $\hat{y} = (\hat{a} + \hat{b})/\sqrt{2}$  (armchair) we reach the AB stacking [in Fig. 2(a)], while along  $\hat{a}$  we reach AB' [in Fig. 2(b)]. In addition we consider several lower-symmetry stacking geometries along the paths connecting AA to AB through the zigzag and armchair directions and AA to AB'. Their geometry (atomic positions and lattice) were optimized by minimizing the forces on the atoms and stress in the cell. We found two stackings along the zigzag path, named AB'2 [in Fig. 2(c)] and AB'3 [in Fig. 2(d)], and the same stacking, named AB'4 [in Fig. 2(e)], along the  $\hat{a}$  and armchair paths.

In order to unveil the lattice stability of these stackings, we calculated their lattice vibrations with a long wavelength (at  $\Gamma$ ). The AB'2 and AB'3 stackings display phonon instabilities with a shear rigid pattern, where the relative layer displacement is along the  $\hat{y}$  direction. The AB'4 stacking displays a soft mode of a shear rigid pattern along the  $\hat{x}$  direction. The AA, AB, and AB' stackings each display two soft modes of a shear rigid pattern, one along  $\hat{x}$  and the other along  $\hat{y}$  (all these patterns are shown in Fig. S1 in the Supplemental Material [57]).

One approach to find a dynamically stable configuration from a dynamically unstable one is to follow the soft mode. We followed the unstable phonons displayed by the AB'2, AB'3, and AB'4 geometries, and we found the AB'' stacking [in Fig. 2(f)], which does not display soft modes, as indicated by its vibrational dispersion [in Fig. S2(a) in the Supplemental Material]. These results suggest that among the considered stackings in this work, only AB'' is expected to be observed in equilibrium under standard conditions. We hope this finding will motivate experimental works to confirm our predictions.

We also considered a bulk ABC-like stacking [53] and found it to display four soft modes with a shear rigid pattern (two along  $\hat{x}$  and two along  $\hat{y}$ , as shown in Fig. S1). We also proposed a corresponding ABC-like configuration for the AB'' stacking. The geometry optimization results of the ABC-like AB'' show that, after 150 steps of geometry optimization, we

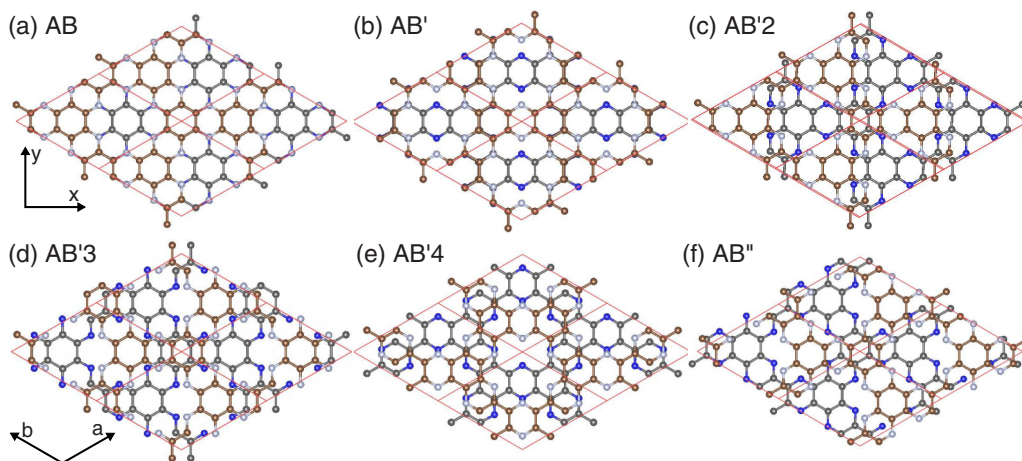


FIG. 2. Bulk C<sub>2</sub>N-h2D geometries found by geometry optimization. Among (a) AB, (b) AB', (c) AB'2, (d) AB'3, (e) AB'4, and (f) AB'', only AB'' does not display phonon instabilities. Carbon and nitrogen atoms in the top (bottom) layer are in brown (gray) and light blue (blue).

TABLE II. Space group (SG), interlayer distance  $d^{\text{vdW}}$  from LDA and rVV10 results, and interlayer binding energy  $E_n$  from rVV10 results for bulk geometries.

Stacking	SG	$d^{\text{vdW}}$ (Å)		$E_n$ (eV/ $n^{\text{vdW}}$ )
		LDA	rVV10	
AA	No. 191 ( $D_{6h}^1$ )	3.44	3.47	-0.645
AB'	No. 69 ( $D_{2h}^{23}$ )	3.14	3.22	-1.102
AB'4	No. 63 ( $D_{2h}^{17}$ )	3.03	3.15	-1.163
AB	No. 194 ( $D_{6h}^4$ )	3.08	3.17	-1.215
ABC	No. 166 ( $D_{3d}^3$ )	2.88	2.98	-1.256
AB'3	No. 63 ( $D_{2h}^{17}$ )	3.00	3.12	-1.256
AB'2	No. 63 ( $D_{2h}^{17}$ )	2.98	3.11	-1.267
AB''	No. 11 ( $C_{2h}^2$ )	2.97	3.10	-1.267

still could not find a structure that satisfies the convergence criteria. These results show that the proposed ABC-like AB'' cannot be an equilibrium geometry. We note that in the search concerning two layers for bulk C<sub>2</sub>N-h2D (36 atoms per unit cell), we started with 136 different geometries, considering cell and atomic position optimization, relative total energies, and lattice dynamics (we highlight we did not address the full energy landscape of the problem). A similar search in three-layer systems (54 atoms per unit cell) would require at least about 136×136 configurations, with no guarantee that a dynamically stable geometry would be found. A search for dynamically stable bulk configurations with more than two layers in the unit cell is beyond the scope of this work.

The comparison of the interlayer binding energies for these bulk stackings (in Table II) reinforces the importance of considering the lattice dynamics of crystals in order to investigate the stability of the geometries. Although some stackings display comparable  $E_n$ , such as AB'' and AB'2 and also AB'3 and ABC, only AB'' does not display soft modes.

The AB'' stacking has low symmetry, belonging to the  $C_{2h}^2$  space group (No. 11 or  $2/m$ ). Our calculations indicate that the  $a$  and  $b$  lattice vectors of its primitive unit cell differ in length by  $\approx 0.01$  Å (bulk data in Table I) and form a  $\gamma$  angle of  $119.92^\circ$  ( $\alpha$  and  $\beta$  are equal to  $90^\circ$ ). Both bulk in-plane lattice vectors are shorter than the monolayer  $a$  (equal to  $b$ ) lattice vector by  $\approx 0.1$  Å (LDA), suggesting the influence of the interlayer interaction on the in-plane structure. The stacking lattice constant  $c$  in layered materials is also systematically underestimated by LDA and overestimated by GGA and vdW functionals, and in general rVV10 is in better agreement with experiments, followed by LDA. The unexpectedly good results of LDA are attributable to error cancellation. Our results show that the experimental value of  $6.55(1)$  Å [22] is underestimated by LDA by  $-0.1\%$  and underestimated by rVV10 by  $-0.07\%$  (bulk data in Table I).

We investigated the corresponding bilayer geometries of the AB, AB'2, and AB'' stacking. The AB bilayer displays two soft modes with a shear rigid pattern, one along  $\hat{x}$  and one along  $\hat{y}$ , and the bilayer AB'2 displays one soft mode with a shear rigid pattern along  $\hat{y}$  as the corresponding bulk geometries (in Fig. S1 in the Supplemental Material) of these two stackings. The bilayer AB'' stacking is dynamically stable,

TABLE III. Space group (SG), interlayer distance  $d^{\text{vdW}}$  from LDA and rVV10 calculations, and interlayer binding energy  $E_n$  from rVV10 calculations for bilayer geometries.

Stacking	SG	$d^{\text{vdW}}$ (Å)		$E_n$ (eV/ $n^{\text{vdW}}$ )
		LDA	rVV10	
AB	No. 164 ( $D_{3d}^3$ )	3.05	3.16	-1.092
AB'2	No. 12 ( $C_{2h}^3$ )	2.95	3.09	-1.129
AB''	No. 2 ( $C_i^1$ )	2.94	3.09	-1.131

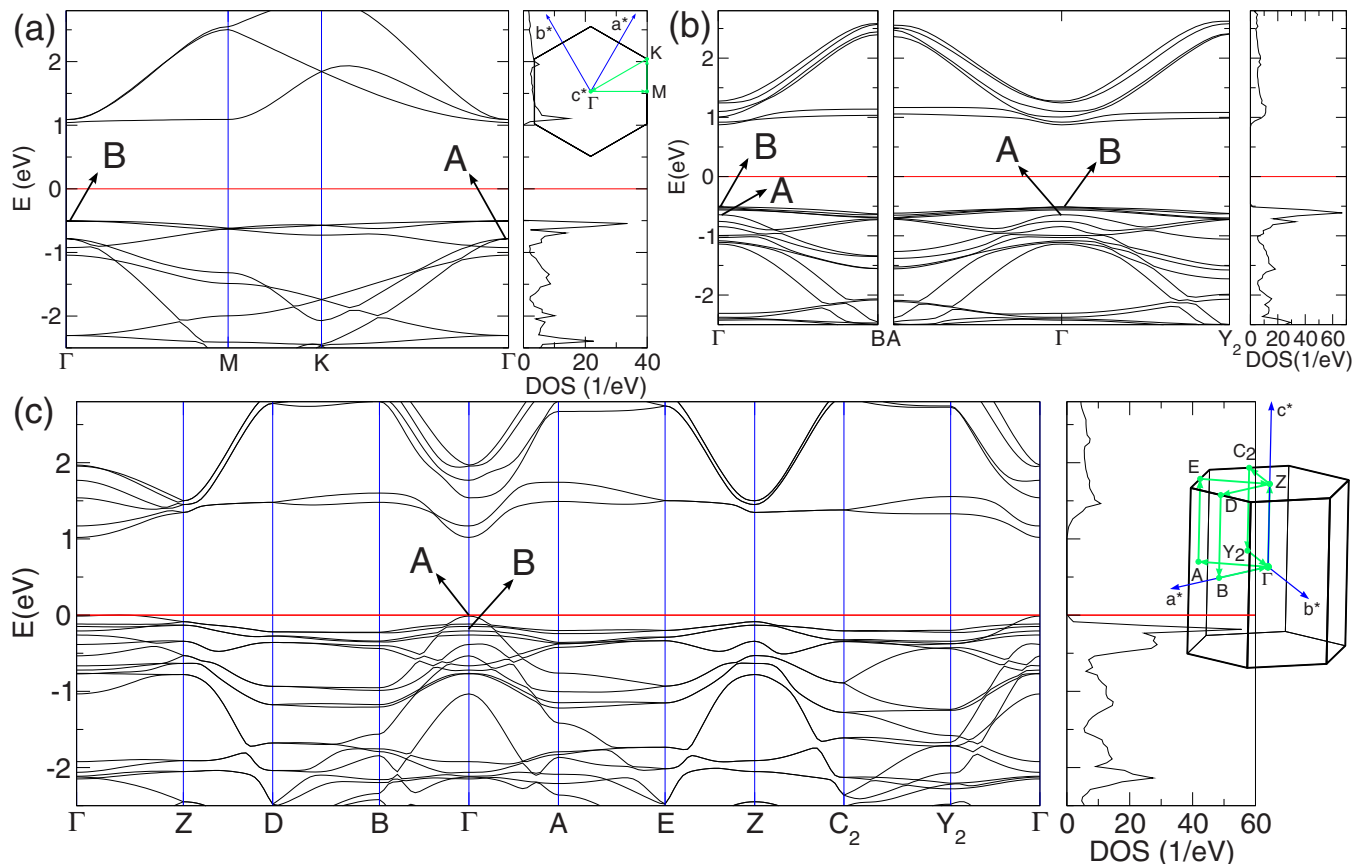
as observed in its vibrational structure [in Fig. S2(b) in the Supplemental Material].  $E_n$  for the bilayer stackings is shown in Table III.

The AB'' bilayer displays lower symmetry compared to the other geometries, belonging to the space group  $C_i^1$ . In this case, the  $a$  and  $b$  lattice vectors are slightly different in size, 10 times smaller than the difference in the bulk (L2 and bulk data in Table I). When going from bilayer to bulk AB'', we note the following trends in rVV10 result: (i) The differences in interlayer distance ( $\Delta d^{\text{vdW}} = d_{\text{bulk}}^{\text{vdW}} - d_{\text{bilayer}}^{\text{vdW}}$ ) slightly increase by  $0.01$  Å; that is, the layers become more distant from each other in bulk. (ii) The differences in the interlayer binding energy [ $\Delta E_n = E_n(\text{bulk}) - E_n(\text{bilayer})$ ] decrease by  $-0.136$  eV/ $n^{\text{vdW}}$ ; that is, the layers become more bound to each other in bulk. As  $\Delta E_n \neq 0$ , rVV10 displays the nonadditivity of the vdW interactions [58–61]. Although we do not expect that rVV10 should correctly describe the nonadditivity of the vdW interactions, as it should not correctly describe many-body effects or electrodynamic effects in the polarizability, the trends of the results are what one would expect ( $\Delta E_n$  should decrease) [61].

Experiments performed with monolayer C<sub>2</sub>N-h2D on top of Cu(111) show a slight buckling (in the  $z$  coordinate). In this case, the pyrazine rings are  $\approx 0.05$  Å below the benzenelike ring formed by the C-C bond linking them [22]. This monolayer buckling must be a surface-induced effect, as in our results for a free monolayer all the atoms are in the same  $z$  coordinate. Also, in AB'' bilayer and bulk, all the atoms of a given layer have the same  $z$  coordinate.

## B. Electronic structure

The electronic structure of layered materials can be largely dependent on the number of layers in the sample. In the next section we discuss the evolution of the electronic structure of C<sub>2</sub>N-h2D from monolayer to bilayer and to the bulk in the dynamically stable stacking order AB''. The band structure [electronic dispersion and density of states (DOS)] of the monolayer, bilayer, and bulk are shown in Figs. 3(a), 3(b), and 3(c), respectively. In the inset of the DOS graphics in Figs. 3(a) and 3(c) we show the first Brillouin zone and the recommended path to be considered (based on the space groups) [62,63] for the monolayer and bulk, respectively. For the bilayer we consider the same paths as in the bulk within the plane  $k_z = 0$ : the  $\overline{\Gamma B}$  and  $\overline{A\Gamma Y_2}$  paths, although these lines have different symmetries in the bilayer than they have in the bulk due to the different space groups indicated in Tables II and III.


 FIG. 3. Electronic structure of dynamically stable C<sub>2</sub>N-h2D geometries. (a) Monolayer, (b) bilayer, and (c) bulk AB'.

### 1. Band gap

We start our analysis by considering the influence of the number of layers on the band gap of C<sub>2</sub>N-h2D. The calculations indicate that the monolayer C<sub>2</sub>N-h2D is a semiconductor, with a direct band gap at  $\Gamma$  of 1.55 eV. In the bilayer it decreases by 16% (to 1.3 eV), and in the bulk it decreases by 34% (to 1.03 eV). In addition, as the number of layers increases, the valence-band maximum (VBM) moves to the  $\overline{\Gamma Z}$ - $\Gamma$  direction, and we found an indirect band gap in the bulk at  $\overline{\Gamma Z}$ - $\Gamma$  of 1.02 eV. This indirect band gap could compete with the direct band gap at  $\Gamma$ . We note that the LDA prediction for the bulk band gap underestimates the experimental value by 48% (available measures were performed in both powder and films and estimated to be 1.96 eV [22]), a well-known issue of standard functionals (LDA, GGA). These results suggest that the direct band gap can be decreased within a large window by controlling the number of layers. This effect can be explored in device engineering in optoelectronics in the visible range.

### 2. Effective masses

We now consider the influence of the number of layers in the effective masses of the conduction and valence bands (the details of the calculation of the effective masses are in the Supplemental Material).

The monolayer lower conduction band displays anisotropy between the  $\overline{\Gamma K}$  ( $\hat{y}$ , armchair) and  $\overline{\Gamma M}$  ( $\hat{x}$ , zigzag) directions, as shown in Fig. 3(a). The electrons in the conduction-band

minimum (CBM), at  $\Gamma$ , display effective masses  $m_e^*$  along  $\overline{\Gamma K}$  and  $\overline{\Gamma M}$  that differ by  $0.02m_e$  (see Table IV). Under an external electric field an electron in the CBM will respond with a positive  $m_e^*$  along the whole path  $\overline{\Gamma K}$  until it is scattered back to near the CBM. Along  $\overline{\Gamma M}$  in  $\approx \overline{\Gamma M}/8$ , only 0.02 eV above the CBM, there is an inflection point in  $E(k)$ , and from this point to the border of the Brillouin zone the electron will respond to the electric field with a negative  $m_e^*$  (the lattice slows down the electron) [64]. This nonparabolic region from  $\approx \overline{\Gamma M}/8$  and beyond may be accessible to the electron before it is scattered back to near the CBM, and its average velocity along  $\overline{\Gamma M}$  should be slower than along  $\overline{\Gamma K}$ . Furthermore, the bandwidth along  $\overline{\Gamma M}$  is 0.05 eV, while the bandwidth along  $\overline{\Gamma K}$  is 0.80 eV,

 TABLE IV. Effective masses (in units of electron mass  $m_e$ ) for electrons and holes for monolayer (L1) and bulk dynamically stable C<sub>2</sub>N-h2D.

	L1		Bulk				
	$\overline{\Gamma M}$	$\overline{\Gamma K}$	$\overline{\Gamma A}$	$\overline{\Gamma B}$	$\overline{\Gamma Z}(\Gamma)$	$\overline{\Gamma Z}(\text{VBM})$	
$m_e^*$	0.12	0.10	0.08	0.08	0.10	0.50	
$m_h^*$	3.81	4.05	0.09	0.10	0.14	1.82	1.70

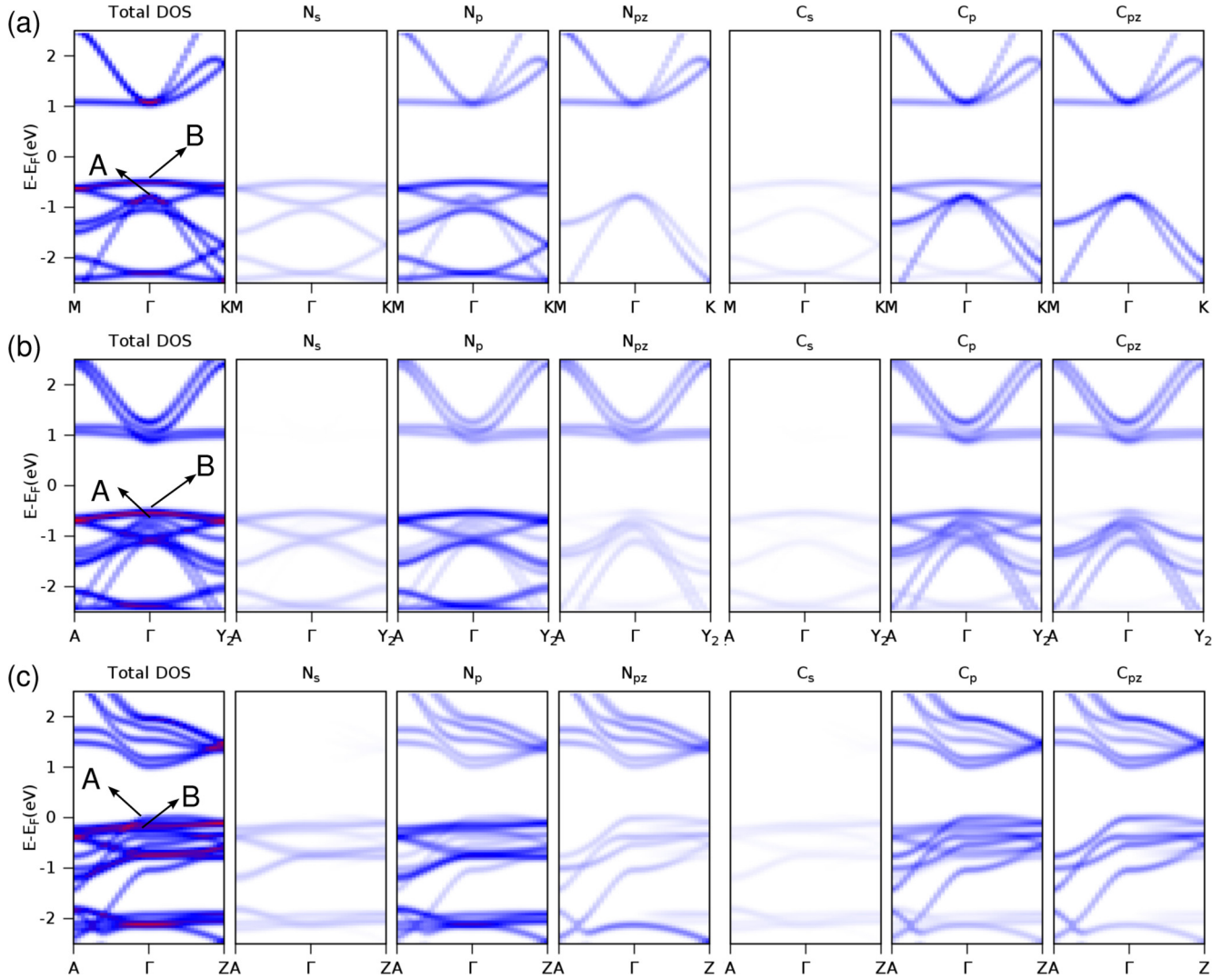


FIG. 4. Color maps of the projected density of states on the bands along selected directions for the dynamically stable  $C_2N$ -h2D geometries. (a) Monolayer, (b) bilayer, and (c) bulk. The transition from null to maximum values follows the white-blue-red palette.

and within a tight-binding picture, where narrow bands indicate low hopping through the lattice, the electron would find it harder to travel along  $\vec{\Gamma M}$  than along  $\vec{\Gamma K}$ . These results suggest that the electron conductivity along  $\vec{\Gamma M}$  should be inferior than that along  $\vec{\Gamma K}$ . The holes display considerably higher effective masses  $m_h^*$  than electrons, by a factor of 35. The  $m_h^*$  also displays anisotropy between the  $\vec{\Gamma K}$  and  $\vec{\Gamma M}$  directions, with a difference of  $0.25m_e$  in the VBM at  $\Gamma$  (see Table IV).

The comparison between the monolayer and bulk electronic dispersion displayed in Figs. 3(a) and 3(c) indicates that the interlayer interaction raises the degeneracy in the valence-band edge at  $\Gamma$ . It also reduces the values of both  $m_e^*$  and  $m_h^*$  (as similarly observed in transition-metal dichalcogenides [65] and phosphorene [66]) and their anisotropy along the in-plane directions (see Table IV). As an example, the  $\vec{\Gamma M}$  direction in the monolayer is equivalent to the  $\vec{\Gamma A}$  direction in the bulk (corresponding to  $\hat{x}$  in real space). Along these directions, from the monolayer to bulk and near  $\Gamma$ ,  $m_e^*$  decreases by  $0.04m_e$  (reaching  $0.08m_e$ ), and the conduction bandwidth

increases by  $0.42$  eV (reaching  $0.47$  eV), while  $m_h^*$  decreases by  $3.72m_e$  (reaching  $0.09m_e$ ). These results indicate that the carrier transport within the in-plane directions may be tuned by controlling the number of layers in the sample.

In bulk, both  $m_e^*$  and  $m_h^*$  along  $\vec{\Gamma Z}$  are higher than along in-plane directions, revealing the 2D character of  $C_2N$ -h2D.

### 3. Valence- and conduction-band orbital composition

We gain further understanding of the band structures by considering their orbital composition. In Figs. 4(a), 4(b), and 4(c), we show the projection of the density of states related to the displayed bands in Figs. 3(a), 3(b) and 3(c), respectively, on the  $2s$  and  $2p$  atomic orbitals of carbon,  $C(s)$  and  $C(p)$ , and nitrogen,  $N(s)$  and  $N(p)$ . In these plots we use color maps with the same scale to unveil the orbital composition of the bands. The transition from a null value to the maximum value follows the white-blue-red palette. From the difference in the  $p$  and  $p_z$  projections, we estimate the in-plane  $p_{x,y}$  contribution. The  $p_z$  projections of carbon and nitrogen atoms are represented as  $C(p_z)$  and  $N(p_z)$ , respectively.

TABLE V. Percentage orbital composition at  $\Gamma$  of the conduction-band minimum (CBM), A and B bands in monolayer (L1), bilayer (L2), and bulk dynamically stable C<sub>2</sub>N-h2D.  $X(s)$ ,  $X(p)$ , and  $X(p_z)$  stand for the  $s$  orbital,  $p$  orbital, and  $p_z$  orbital, respectively, from atom  $X = \text{C}$  or  $\text{N}$ . VBM in parentheses after the A or B band indicates the valence-band maximum.

	Band	Orbital composition (%)					
		N( $s$ )	N( $p_{x,y}$ )	N( $p_z$ )	C( $s$ )	C( $p_{x,y}$ )	C( $p_z$ )
L1	CBM	0	0	46	0	0	54
	A	0	0	19	0	0	81
	B (VBM)	10	62	0	3	25	0
L2	CBM	0	0	32	0	0	68
	A	1	4	20	0	1	74
	B (VBM)	8	52	3	3	21	13
Bulk	CBM	0	0	27	0	0	73
	A (VBM)	1	6	17	0	2	74
	B	9	62	0	3	26	0

In the case of monolayer C<sub>2</sub>N-h2D [in Fig. 4(a)], the CBM comes from only  $p_z$  orbitals, where the contribution from C( $p_z$ ) is higher than the contribution from N( $p_z$ ). The B band (VBM), indicated in Fig. 4(a), displays only  $p_{x,y}$  and  $s$  character, where N( $p_{x,y}$ ) is predominant. The A band, indicated in Fig. 4(a), displays only  $p_z$  character, where the contribution from C( $p_z$ ) is considerably larger than the contribution from N( $p_z$ ).

From monolayer to bilayer [in Fig. 4(b)] and to bulk [in Fig. 4(c)] we notice the following trends: The CBM keeps its pure  $p_z$  character, and the contribution from C( $p_z$ ) tends to increase over the contribution from N( $p_z$ ). The interlayer interaction induces the overlap of the A and B bands. The VBM gains contributions from  $p_z$  orbitals, large ones from C( $p_z$ ), and the contributions from  $p_{x,y}$  and  $s$  of both carbon and nitrogen decrease.

The increase in the C( $p_z$ ) contribution to valence and conduction bands as the number of layers increases results in the reduction of both carrier effective masses and their in-plane anisotropy and a reduction of the band gap. These results provide insight into the development of Hamiltonian models based on orbital band composition to further study the band structure of C<sub>2</sub>N-h2D. We summarize the percentage band orbital composition at  $\Gamma$  in Table V.

In monolayer C<sub>2</sub>N-h2D, the assessment of the orbital composition of the VBM from plots of the local density of states (LDOS) calculated with LDA or GGA [22,53] is in agreement with the results in Table V. In the screened hybrid functional of Heyd, Scuseria and Ernzerhof (HSE06) calculations the LDOS of the VBM indicates it is composed of  $p_z$  orbitals from both carbon and nitrogen atoms, while the LDOS of the band below it in energy indicates it is composed of  $p_{x,y}$  orbitals from

carbon and nitrogen atoms [33]. The exact exchange fraction incorporated by a parameter in HSE06 pushes up the  $p_z$  band in energy (A band) in comparison to the  $p_{x,y}$  band (B band) [33], which is thus inverted in comparison to LDA and GGA results. On the other hand, the lower conduction bands obtained by LDA, GGA, and HSE are in agreement [22,33,53]. We expect that the trends in band gap and effective-mass changes when the number of layers increases, as obtained with LDA, will also be observed in HSE06 results. A detailed comparison of the bands calculated with standard and hybrid functionals and a study of the optimum exchange parameter in HSE06 for C<sub>2</sub>N-h2D systems [67] are beyond the scope of this work.

#### IV. CONCLUSION

In this work, we theoretically investigated the phonon stability of several bulk C<sub>2</sub>N-h2D polytypes. Among the polytypes addressed, only AB'' is expected to be observed in equilibrium under standard conditions, as only it does not display phonon instabilities. In addition, we showed that its bilayer counterpart is also dynamically stable. We unveiled the evolution of the electronic structure of the C<sub>2</sub>N-h2D from monolayer to bilayer and then to bulk AB'' stacking. We found that the direct band gap at  $\Gamma$  can be reduced by 34% when going from monolayer to bulk, offering opportunities to tune this property for optoelectronics. The increase in the number of layers reduces the effective masses of both carriers and the anisotropy of the conduction and valence bands along the in-plane directions displayed in the monolayer. This suggests that the transport of carriers may be tuned by controlling the number of layers as well. These results are needed to broaden the understanding of experimental work being performed in this new material, especially for fundamental aspects such as its electronic and phonon dispersion, as well as its structural characterization and property optimization for further device fabrication.

#### ACKNOWLEDGMENTS

The authors thank the Foundation for Research Support of Minas Gerais (FAPEMIG Grants No. CEX-APQ-01865-17, No. TEC-AUC-00026-16, No. RED-00185-16, No. RED-00282-16), and the National Council for Scientific and Technological Development (CNPq Grant No. 310813/2017-4), and the Agency for Financing Studies and Projects - FINEP (02/2014 DMOL No. 0058/16 and NANO No. 0501/16, and 02/2016) for the financial and equipment support to this work. J.R-S. acknowledges support from the Pró-Reitoria de Pesquisa and Pró-Reitoria de Gestão (UFLA) and the prize L'ORÉAL-UNESCO-ABC Prêmio Para Mulheres na Ciência (For Women in Science Prize - Brazil/2017). R.L. acknowledges computational time at CENAPAD-SP, CENAPAD-RJ/LNCC, DFI-UFLA and LCC-UFLA.

- [1] K. S. Novoselov, A. K. Geim, S. V. Morozov, D. Jiang, Y. Zhang, S. V. Dubonos, I. V. Grigorieva, and A. A. Firsov, *Science* **306**, 666 (2004).  
 [2] K. S. Novoselov, A. K. Geim, S. V. Morozov, D. Jiang, I. V. Grigorieva, S. V. Dubonos, and A. A. Firsov, *Nature (London)* **438**, 197 (2005).

- [3] M. I. Katsnelson, K. S. Novoselov, and A. K. Geim, *Nat. Phys.* **2**, 620 (2006).  
 [4] A. H. Castro Neto and K. Novoselov, *Rep. Prog. Phys.* **74**, 082501 (2011).  
 [5] J. Ribeiro-Soares and M. S. Dresselhaus, *Braz. J. Phys.* **44**, 278 (2013).

- [6] A. K. Geim and I. V. Grigorieva, *Nature (London)* **499**, 419 (2013).
- [7] K. F. Mak, C. Lee, J. Hone, J. Shan, and T. F. Heinz, *Phys. Rev. Lett.* **105**, 136805 (2010).
- [8] Q. H. Wang, K. Kalantar-Zadeh, A. Kis, J. N. Coleman, and M. S. Strano, *Nat. Nanotechnol.* **7**, 699 (2012).
- [9] G. Fiori, F. Bonaccorso, G. Iannaccone, T. Palacios, D. Neumaier, A. Seabaugh, S. K. Banerjee, and L. Colombo, *Nat. Nanotechnol.* **9**, 768 (2014).
- [10] G. Ding, G. Gao, and K. Yao, *Sci. Rep.* **5**, 9567 (2015).
- [11] J. P. Heremans, M. S. Dresselhaus, L. E. Bell, and D. T. Morelli, *Nat. Nanotechnol.* **8**, 471 (2013).
- [12] P. D. Antunez, J. J. Buckley, and R. L. Brutchey, *Nanoscale* **3**, 2399 (2011).
- [13] H. L. Zhuang and R. G. Hennig, *Chem. Mater.* **25**, 3232 (2013).
- [14] R. K. Singh, R. Kumar, and D. P. Singh, *RSC Adv.* **6**, 64993 (2016).
- [15] Z. Zhao, Y. Sun, and F. Dong, *Nanoscale* **7**, 15 (2015).
- [16] E. Kroke, M. Schwarz, E. Horath-Bordon, P. Kroll, B. Noll, and A. D. Norman, *New J. Chem.* **26**, 508 (2002).
- [17] E. Kroke and M. Schwarz, *Coord. Chem. Rev.* **248**, 493 (2004).
- [18] A. Schwarzer, T. Saplinova, and E. Kroke, *Coord. Chem. Rev.* **257**, 2032 (2013).
- [19] W. H. Brito, J. da Silva-Araújo, and H. Chacham, *J. Phys. Chem. C* **119**, 19743 (2015).
- [20] X. Wang, K. Maeda, A. Thomas, K. Takanabe, G. Xin, J. M. Carlsson, K. Domen, and M. Antonietti, *Nat. Mater.* **8**, 76 (2009).
- [21] Q. Guo, Q. Yang, C. Yi, L. Zhu, and Y. Xie, *Carbon* **43**, 1386 (2005).
- [22] Javeed Mahmood, Eun Kwang Lee, Minbok Jung, Dongbin Shin, In-Yup Jeon, Sun-Min Jung, Hyun-Jung Choi, Jeong-Min Seo, Seo-Yoon Bae, So-Dam Sohn, Noejung Park, Joon Hak Oh, Hyung-Joon Shin, and Jong-Beom Baek, *Nat. Commun.* **6**, 6486 (2015).
- [23] K. S. Novoselov, D. Jiang, F. Schedin, T. J. Booth, V. V. Khotkevich, S. V. Morozov, and A. K. Geim, *Proc. Natl. Acad. Sci. USA* **102**, 10451 (2005).
- [24] B. Radisavljevic, A. Radenovic, J. Brivio, V. Giacometti, and A. Kis, *Nat. Nanotechnol.* **6**, 147 (2011).
- [25] A. Hashmi, M. U. Farooq, I. Khan, J. Son, and J. Hong, *J. Mater. Chem. A* **5**, 2821 (2017).
- [26] Y. Yang, W. Li, H. Zhou, X. Zhang, and M. Zhao, *Sci. Rep.* **6**, 29218 (2016).
- [27] L. Zhu, Q. Xue, X. Li, T. Wu, Y. Jin, and W. Xing, *J. Mater. Chem. A* **3**, 21351 (2015).
- [28] B. Xu, H. Xiang, Q. Wei, J. Q. Liu, Y. D. Xia, J. Yin, and Z. G. Liu, *Phys. Chem. Chem. Phys.* **17**, 15115 (2015).
- [29] Y. Qu, F. Li, H. Zhou, and M. Zhao, *Sci. Rep.* **6**, 19952 (2016).
- [30] B. Mortazavi, O. Rahaman, T. Rabczuk, and L. F. C. Pereira, *Carbon* **106**, 1 (2016).
- [31] H. Sahin, *Phys. Rev. B* **92**, 085421 (2015).
- [32] J. Du, C. Xia, T. Wang, W. Xiong, and J. Li, *J. Mater. Chem. C* **4**, 9294 (2016).
- [33] S. Guan, Y. Cheng, C. Liu, J. Han, Y. Lu, S. A. Yang, and Y. Yao, *Appl. Phys. Lett.* **107**, 231904 (2015).
- [34] P. Hohenberg and W. Kohn, *Phys. Rev.* **136**, B864 (1964).
- [35] W. Kohn and L. J. Sham, *Phys. Rev.* **140**, A1133 (1965).
- [36] S. Baroni, S. de Gironcoli, A. Dal Corso, and P. Giannozzi, *Rev. Mod. Phys.* **73**, 515 (2001).
- [37] P. Giannozzi, S. Baroni, N. Bonini, M. Calandra, R. Car, C. Cavazzoni, D. Ceresoli, G. L. Chiarotti, M. Cococcioni, I. Dabo, A. D. Corso, S. de Gironcoli, S. Fabris, G. Fratesi, R. Gebauer, U. Gerstmann, C. Gougousis, A. Kokalj, M. Lazzeri, L. Martin-Samos, N. Marzari, F. Mauri, R. Mazzarello, S. Paolini, A. Pasquarello, L. Paulatto, C. Sbraccia, S. Scandolo, G. Sclauzero, A. P. Seitsonen, A. Smogunov, P. Umari, and R. M. Wentzcovitch, *J. Phys.: Condens. Matter* **21**, 395502 (2009).
- [38] H. J. Monkhorst and J. D. Pack, *Phys. Rev. B* **13**, 5188 (1976).
- [39] J. P. Perdew and A. Zunger, *Phys. Rev. B* **23**, 5048 (1981).
- [40] N. Troullier and J. L. Martins, *Phys. Rev. B* **43**, 1993 (1991).
- [41] L. He, F. Liu, G. Hautier, M. J. T. Oliveira, M. A. L. Marques, F. D. Vila, J. J. Rehr, G.-M. Rignanese, and A. Zhou, *Phys. Rev. B* **89**, 064305 (2014).
- [42] J. Serrano, A. Bosak, R. Arenal, M. Krisch, K. Watanabe, T. Taniguchi, H. Kanda, A. Rubio, and L. Wirtz, *Phys. Rev. Lett.* **98**, 095503 (2007).
- [43] T. Kuzuba, K. Era, T. Ishii, and T. Sato, *Solid State Commun.* **25**, 863 (1978).
- [44] R. J. Nemanich, S. A. Solin, and R. M. Martin, *Phys. Rev. B* **23**, 6348 (1981).
- [45] Y. Zhao, X. Luo, H. Li, J. Zhang, P. T. Araujo, C. K. Gan, J. Wu, H. Zhang, S. Y. Quek, M. S. Dresselhaus, and Q. Xiong, *Nano Lett.* **13**, 1007 (2013).
- [46] A. Molina-Sánchez and L. Wirtz, *Phys. Rev. B* **84**, 155413 (2011).
- [47] R. Sabatini, T. Gorni, and S. de Gironcoli, *Phys. Rev. B* **87**, 041108 (2013).
- [48] R. Sabatini, E. Küçükbenli, C. H. Pham, and S. de Gironcoli, *Phys. Rev. B* **93**, 235120 (2016).
- [49] O. A. Vydrov and T. Van Voorhis, *J. Chem. Phys.* **133**, 244103 (2010).
- [50] P. E. Blöchl, *Phys. Rev. B* **50**, 17953 (1994).
- [51] A. Dal Corso, *Comput. Mater. Sci.* **95**, 337 (2014).
- [52] *International Tables for Crystallography*, 5th ed., *Space-Group Symmetry*, edited by T. Hahn (Springer, Dordrecht, 2005), Vol. A.
- [53] R. Zhang, B. Li, and J. Yang, *Nanoscale* **7**, 14062 (2015).
- [54] P. Anees, M. C. Valsakumar, S. Chandra, and B. K. Panigrahi, *Modell. Simul. Mater. Sci. Eng.* **22**, 035016 (2014).
- [55] G. Savini, Y. Dappe, S. Öberg, J.-C. Charlier, M. Katsnelson, and A. Fasolino, *Carbon* **49**, 62 (2011).
- [56] S. Scandolo, M. Bernasconi, G. L. Chiarotti, P. Focher, and E. Tosatti, *Phys. Rev. Lett.* **74**, 4015 (1995).
- [57] See Supplemental Material at <http://link.aps.org/supplemental/10.1103/PhysRevB.97.195119> for effective masses calculations, image of unstable phonon modes, and graphics of phonon dispersion of stable bilayer and bulk C<sub>2</sub>N-h2D geometries.
- [58] V. V. Gobre and A. Tkatchenko, *Nat. Commun.* **4**, 2341 (2013).
- [59] C. Wagner, N. Fournier, V. G. Ruiz, C. Li, K. Müllen, M. Rohlfing, A. Tkatchenko, R. Temirov, and F. S. Tautz, *Nat. Commun.* **5**, 5568 (2014).
- [60] J. Tao and J. P. Perdew, *J. Chem. Phys.* **141**, 141101 (2014).
- [61] L. Shulenburg, A. Baczewski, Z. Zhu, J. Guan, and D. Tománek, *Nano Lett.* **15**, 8170 (2015).
- [62] *Space Groups and Their Representations*, edited by G. Koster (Academic Press, New York, 1957).
- [63] Y. Hinuma, G. Pizzi, Y. Kumagai, F. Oba, and I. Tanaka, *Comput. Mater. Sci.* **128**, 140 (2017).



- [64] C. Kittel, *Introduction to Solid State Physics* (Wiley, Hoboken, NJ, 2005).
- [65] W. S. Yun, S. W. Han, S. C. Hong, I. G. Kim, and J. D. Lee, *Phys. Rev. B* **85**, 033305 (2012).
- [66] J. Qiao, X. Kong, Z.-X. Hu, F. Yang, and W. Ji, *Nat. Commun.* **5**, 4475 (2014).
- [67] M. A. L. Marques, J. Vidal, M. J. T. Oliveira, L. Reining, and S. Botti, *Phys. Rev. B* **83**, 035119 (2011).